



HAL
open science

Evidence for correlated electron pairs and triplets in quantum Hall interferometers

Wenmin Yang, David Perconte, Corentin Déprez, Kenji Watanabe, Takashi Taniguchi, Sylvain Dumont, Edouard Wagner, Frédéric Gay, Inès Safi, Hermann Sellier, et al.

► To cite this version:

Wenmin Yang, David Perconte, Corentin Déprez, Kenji Watanabe, Takashi Taniguchi, et al.. Evidence for correlated electron pairs and triplets in quantum Hall interferometers. *Nature Communications*, 2024, 15, pp.10064. <10.1038/s41467-024-54211-3>. <hal-04799999v2>

HAL Id: hal-04799999

<https://hal.science/hal-04799999v2>

Submitted on 23 Nov 2024

HAL is a multi-disciplinary open access archive for the deposit and dissemination of scientific research documents, whether they are published or not. The documents may come from teaching and research institutions in France or abroad, or from public or private research centers.

L'archive ouverte pluridisciplinaire HAL, est destinée au dépôt et à la diffusion de documents scientifiques de niveau recherche, publiés ou non, émanant des établissements d'enseignement et de recherche français ou étrangers, des laboratoires publics ou privés.




Distributed under a Creative Commons CC BY-NC-ND 4.0 - Attribution - Non-commercial use - No Derivative Works - International License

Evidence for correlated electron pairs and triplets in quantum Hall interferometers

Received: 25 July 2024

Accepted: 31 October 2024

Published online: 20 November 2024

 Check for updates

Wenmin Yang^{1,5}, David Perconte^{1,5}, Corentin Déprez¹, Kenji Watanabe^{1,2}, Takashi Taniguchi³, Sylvain Dumont¹, Edouard Wagner¹, Frédéric Gay¹, Inès Safi⁴, Hermann Sellier¹ & Benjamin Sacépé¹ ✉

The pairing of electrons is ubiquitous in electronic systems featuring attractive inter-electron interactions, as exemplified in superconductors. Counter-intuitively, it can also be mediated in certain circumstances by the repulsive Coulomb interaction alone. Quantum Hall (QH) Fabry–Pérot interferometers (FPIs) tailored in a two-dimensional electron gas under a perpendicular magnetic field have been argued to exhibit such an unusual electron pairing, seemingly without attractive interactions. Here, we show evidence in graphene QH FPIs, revealing not only a similar electron pairing at bulk filling factor $\nu_B = 2$, but also an unforeseen emergence of electron tripling characterized by a fractional Aharonov–Bohm flux period of $h/3e$ (h is the Planck constant and e the electron charge) at $\nu_B = 3$. Leveraging plunger–gate spectroscopy, we demonstrate that electron pairing (tripling) involves correlated charge transport on two (three) entangled QH edge channels. This spectroscopy indicates a quantum interference flux periodicity determined by the sum of the phases acquired by the distinct QH edge channels having slightly different interfering areas. Phase jumps observed in the pajama maps can be accounted for by the frequency beating between pairing/tripling modes and the outer interfering edge.

The quantum Hall effect is known to host a wide range of correlated and symmetry-protected phases. Coulomb repulsion plays a central role in it, shaping the structure of QH edge channels¹, inducing (pseudo) spin-polarized QH ferromagnets², or generating fractional quantum Hall states³ with anyonic excitations that may be useful for topological quantum computation⁴.

In 2015, a surprise came with the observation of the pairing of electrons in QH interferometers. Choi and co-workers⁵ found in GaAs Fabry–Pérot interferometers (FPIs) defined by two quantum point contacts (QPCs) in series⁶ an anomalous Aharonov–Bohm (AB) effect with halved flux-periodicity, $h/2e$. The specific configurations identified were the presence of at least two QH edge channels in the FPI, that

is, a bulk filling factor $\nu_B > 2$, and interference from the outer channel while the inner one forms a closed loop. Strikingly, this electron pairing was confirmed by quantum shot noise that evidenced an effective charge $e^* = 2e$ (refs. 5,7), pointing conspicuously toward correlated electron–pair transport.

The analogy with Cooper pairing in superconductors is tantalizing, however, the resemblance is only apparent since there are no attractive, non-Coulombic interactions, nor evidence of a macroscopic condensate. On the theoretical front, most efforts to date have failed to describe this baffling phenomenon^{8–10}. Yet, an effective dynamical pairing via the exchange of neutralons¹⁰ has been put forward, but cannot capture all phenomenology^{5,7,11}.

¹Univ. Grenoble Alpes, CNRS, Grenoble INP, Institut Néel, Grenoble, France. ²Research Center for Functional Materials, National Institute for Materials Science, Tsukuba, Japan. ³International Center for Materials Nanoarchitectonics, National Institute for Materials Science, Tsukuba, Japan. ⁴Université Paris-Saclay, CNRS, Laboratoire de Physique des Solides, Orsay, France. ⁵These authors contributed equally: Wenmin Yang, David Perconte.

✉ e-mail: benjamin.sacepe@neel.cnrs.fr

Here, we opt for a different platform—the graphene QH FPI^{12–15} to uncover new insights into this phenomenon. By leveraging the high-tunability of its plunger gate¹² and conducting systematic out-of-equilibrium transport measurements, we establish a new QH edge channel spectroscopy that allows us to identify the exact channels involved coherently in the electron pairing. This spectroscopy allows us to conclude that pairing consistently occurs when the number of edge channels exceeds one. The pairing's weight significantly grows with an increase in the filling factor, ultimately leading to visible frequency beating in the pajama map at a filling factor higher than 2. Furthermore, at filling factor $\nu_B = 3$, we uncover evidence of correlated transport involving three electrons over the three distinguishable edge channels. Our systematic exploration of the flux and energy bias parameter space gives key insights into a complex interplay between edge channels and their interactions.

The QH FPIs are made with hBN-encapsulated graphene deposited onto a graphite gate acting as a back-gate electrode. Two QPCs are electrostatically defined by a set of two palladium split-gate electrodes^{12,16}. The FPIs are equipped with a plunger-gate electrode to tune the effective area enclosed by the QH edge channels. Several 1D ohmic contacts¹⁷ allow us to source and drain current and probe voltages across the FPI. Figure 1a shows an atomic force microscopy topography of the device studied in the main text, which has an FPI cavity area of $2.2 \pm 0.2 \mu\text{m}^2$. Importantly, the FPI is defined by the pristine, non-etched edges of the graphene flake, ensuring confinement of the QH edge channels to within a few magnetic lengths of the crystal edge, without any edge reconstruction¹⁸, as well as by split and plunger gates. All experiments are performed at a magnetic field of 14 T and a temperature of 0.01 K. Partial pinch-off of the inner channel as overlaid in Fig. 1a, b yields conductance oscillations shown in Fig. 1c with negative slope in the magnetic field, B , versus plunger gate voltage, V_{pg} , plane, which is characteristic of AB quantum interference for a flux periodicity of h/e ^{12,19}.

Results

Gate-spectroscopy fingerprint of QH edge channels

The considerable advantage of graphene FPI over conventional semiconductors is the absence of a bandgap, which allows one to achieve a very large electrostatic tuning of the charge carrier density ranging from the electron states to the hole states. Figure 1g illustrates this tunability with conductance oscillations versus plunger-gate voltage, V_{pg} , from -5 to 0V , reflecting the quantum interference of the inner channel at $\nu_B = 2$ (same configuration as in Fig. 1a, b). The Fourier transform of these oscillations in a small sliding window gives the plunger-gate dependence of the oscillation frequency¹². The resulting gate-spectroscopy shown in Fig. 1h reveals three peaks of decreasing amplitudes (see inset) that relate to the first harmonic frequency f_{pg} and the next two harmonics $2f_{\text{pg}}$ and $3f_{\text{pg}}$. This indicates quantum interference occurring over two and three turns of the inner channel loop, thus providing a clear signature of the interferometer's high coherence. Importantly, each peak diverges at the same plunger gate voltage $V_{\text{pg}}^c = -0.28\text{V}$, which corresponds to the expulsion of the inner channel from under the gate when the filling factor under the gate reaches $\nu_{\text{pg}} = 1$. This divergence is channel-specific¹² and provides an unambiguous indicator of the QH edge channels involved in the interference.

One new aspect of our measurement approach is the systematic acquisition of IV curves at every point of the interference patterns in Fig. 1c, g, enabling us to simultaneously explore the complete parameter space of energy, plunger gate voltage, and magnetic field (see the plunger gate-dependent oscillations at various bias voltages in Supplementary Movie 1). Figure 1c, g are extracted from the bias-dependence data at zero bias. The bias voltage dependence of the oscillation frequency yields a checkerboard pattern illustrated in Fig. 1e in a restricted gate voltage range, reflecting the additional phase

shift acquired by the injected electrons at finite energy. This checkerboard pattern can be accurately simulated in Fig. 1f, as outlined in the Methods section. In turn, this enables us to compute the Fourier transform of the oscillations at each bias voltage (see oscillation frequency dispersion at various bias voltages in Supplementary Movie 2) and to extract the bias voltage dependence of each harmonic displayed in Fig. 1i. The resulting oscillatory lobe structure of each harmonic is best fitted with a Gaussian decay for the energy relaxation (see ref. 12), and provides the Thouless energy of the interferometer edge $E_{\text{Th}} = h\nu/L = 135 \pm 4 \mu\text{V}$ (bias-oscillation period), where $L = 3.4 \pm 0.2 \mu\text{m}$ is the length of the interfering channel between two QPCs and ν is the edge velocity. The harmonics then yield E_{Th}/N (see Fig. 1i inset), where N is the respective harmonic index, providing an assessment of $\nu = (1.1 \pm 0.1) \times 10^5 \text{ms}^{-1}$ consistent with our previous work¹².

Electron pairing on two coherently coupled channels

Electron pairing emerges in our interferometer in the presence of two edge channels by interfering with the outer channel while keeping the inner channel localized in the interferometer cavity (see inset schematics in Fig. 2a). Gate spectroscopy shown in Fig. 2a reveals the pairing frequency (orange dashed line) that is almost twice that of the inner channel interference unveiled previously in Fig. 1h. Since an area variation of one flux quantum at a fixed magnetic field is $\Delta A = \phi_0/B = \alpha \Delta V_{\text{pg}} = \alpha/f_{\text{pg}}$, where α is the (non-linear) lever arm of the gate and $\Delta V_{\text{pg}} = 1/f_{\text{pg}}$ the plunger-gate oscillation period, a frequency doubling therefore signals an abnormal flux periodicity of $h/2e$ similar to that reported in GaAs^{5,7,11}.

The frequency doubling is also evidenced by the presence of a residual peak at half the frequency highlighted with a red dashed line that coincides with the frequency of the outer channel h/e -periodic interference, the latter being independently characterized by its spectroscopy at a different filling factor where pairing is sub-dominant (Supplementary Fig. 9). Inspecting the plunger-gate evolution of those frequencies, we see that both pairing and outer channel frequencies diverge at $V_{\text{pg}}^c = -0.96\text{V}$, a value corresponding to a filling factor underneath the plunger gate $\nu_{\text{pg}} = 0.05$, in agreement with the expulsion of the outer channel from the plunger gate area.

However, unlike the harmonics in Fig. 1h, the pairing frequency is not exactly twice that of the outer channel: At $V_{\text{pg}} = -4.8\text{V}$, one finds 105V^{-1} and 45V^{-1} , respectively. To understand this discrepancy we add on the gate-spectroscopy the inner channel frequency (first harmonic measured in Fig. 1h) as a black dashed line in Fig. 2a, which leads us to a central finding of this study: The pairing frequency is not double the AB frequency but the sum of the distinct inner and outer channel frequencies. This is seen with the orange dashed line in Fig. 2a, which is constructed from the sum of the black (inner channel) and red (outer channel) dashed lines, and which fits remarkably well with the pairing frequency dispersion. Here the different frequencies for the inner and outer channels stem from their slightly different positions with respect to the plunger and QPC split gates, as discussed in the following, and thus their different effective areas.

This finding is particularly striking and insightful as it demonstrates that, although localized, the inner channel influences the quantum interference of the outer channel and such an unusual pairing frequency. The system therefore behaves as if a correlated excitation propagates on both inner and outer channels, thereby accumulating the sum of the AB phases of both channels $\varphi = \frac{h}{e} \oint_{\text{inner}} \mathbf{A} \cdot d\mathbf{l} + \frac{h}{e} \oint_{\text{outer}} \mathbf{A} \cdot d\mathbf{l}$, where \mathbf{A} is the vector potential.

Examining the bias voltage-dependence of this gate-spectroscopy displayed in Fig. 2b shows that the pairing mode and the outer channels exhibit nearly the same bias voltage periodicity, that is, Thouless energy, confirming the fact that the pairing frequency is not a harmonic of the outer channel interference. Here, it is evident

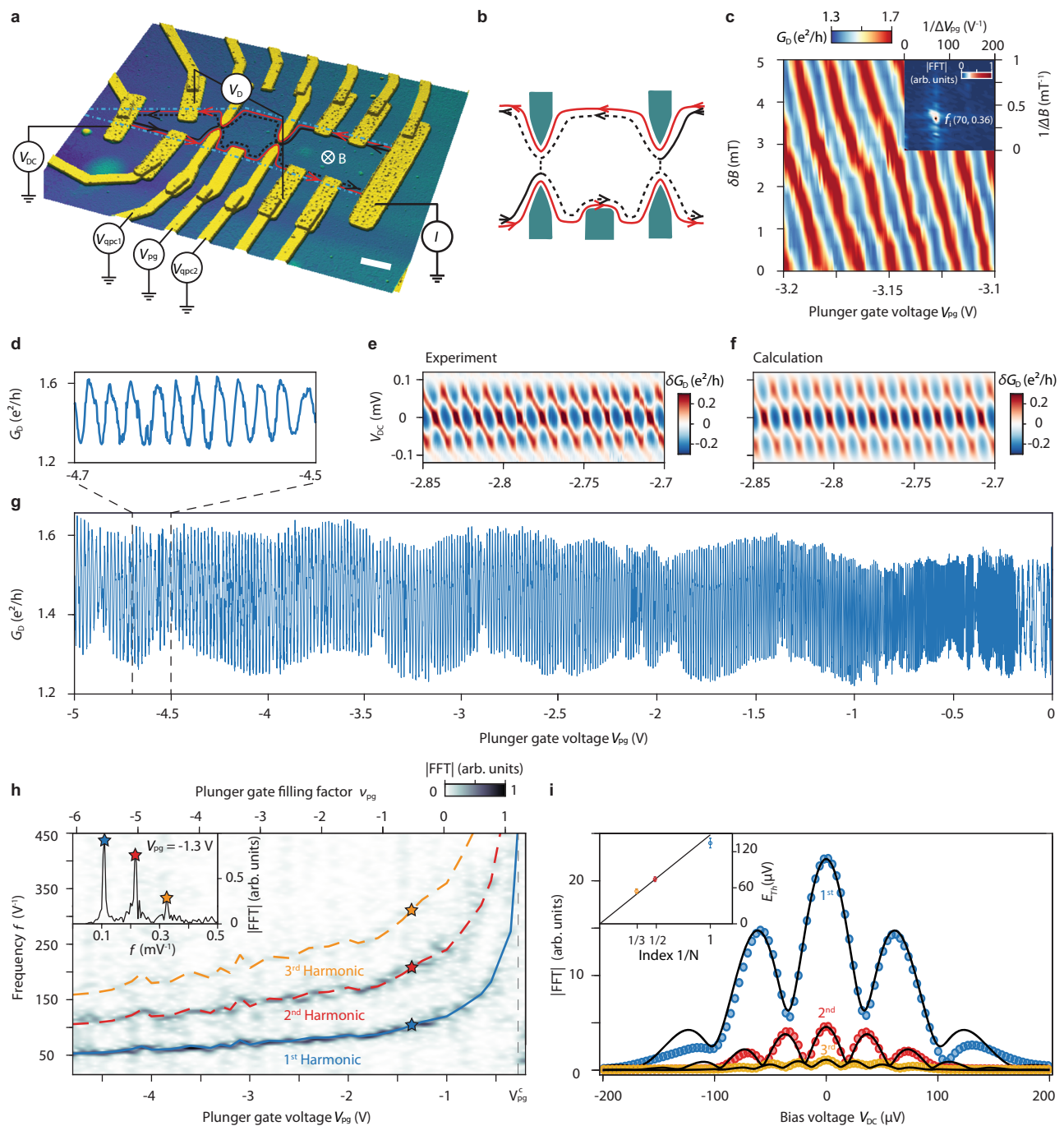


Fig. 1 | Inner edge channel interference at $V_{bg} = 1.8$ V ($\nu_B = 2.26$). **a** Atomic force microscope image of hBN encapsulated graphene. Ohmic contacts (rough surface), plunger gate and quantum point contact (QPC, smooth surface) are in yellow. Inner and outer edges are depicted with black and red. Dashed blue line marks invisible graphene. Diagonal conductance $G_D = I/V_D$, where I and V_D are current and diagonal voltage. Scale is $1 \mu\text{m}$. **b** Schematic of edge configuration. **c** Pajama map, with QPC transmission $T_1 = 0.67$ and $T_2 = 0.66$, reveals AB-dominated interference¹⁹. Inset: Fast Fourier transform (FFT). **d** G_D versus V_{pg} from -4.7 V to

-4.5 V at zero bias V_{DC} . **e, f** Checkerboard extracted from Supplementary Movie 1, and its calculated counterpart (Methods). **g** Oscillations at $0 < V_{pg} < -5$ V, with bias dependence in Supplementary Movie 1. **h** Gate spectroscopy, sliding FT (with a 0.175 V window) on oscillations at $V_{DC} = -28 \mu\text{V}$. Full bias dependence in Supplementary Movie 2. First harmonic (blue line) diverges at V_{pg}^c ; second and third harmonics in dashed red and yellow. Inset: FFT at $V_{pg} = -1.3$ V shows three frequency peaks. **i**, Lobe structures: first (blue), second (red), and third (yellow) harmonic (Methods). Inset: Thouless energy E_{Th} versus inverse harmonic index.

that pairing prevails over the h/e -periodic contribution from the outer channel.

We delve further into the evolution of pairing with respect to changes in filling factor and bias voltage in Supplementary Fig. 9. At a low filling factor ($V_{bg} = 1.2$ V, $\nu_B = 1.7$), pairing is present but with notably lower prominence at all bias voltages (Supplementary Fig. 9a,d). However, pairing significance increases and becomes

dominant as the filling factor rises (Supplementary Fig. 9b, c, e, f). The influence of bias voltage on the relative weight of each frequency becomes particularly noticeable when pairing and outer frequencies have similar amplitudes, as observed at $V_{bg} = 1.58$ V ($\nu_B = 2$, Supplementary Fig. 9e).

Notably, the zero-bias pajama map depicted in Fig. 2c displays a distinct discontinuity in the tilted AB constant phase lines, deviating

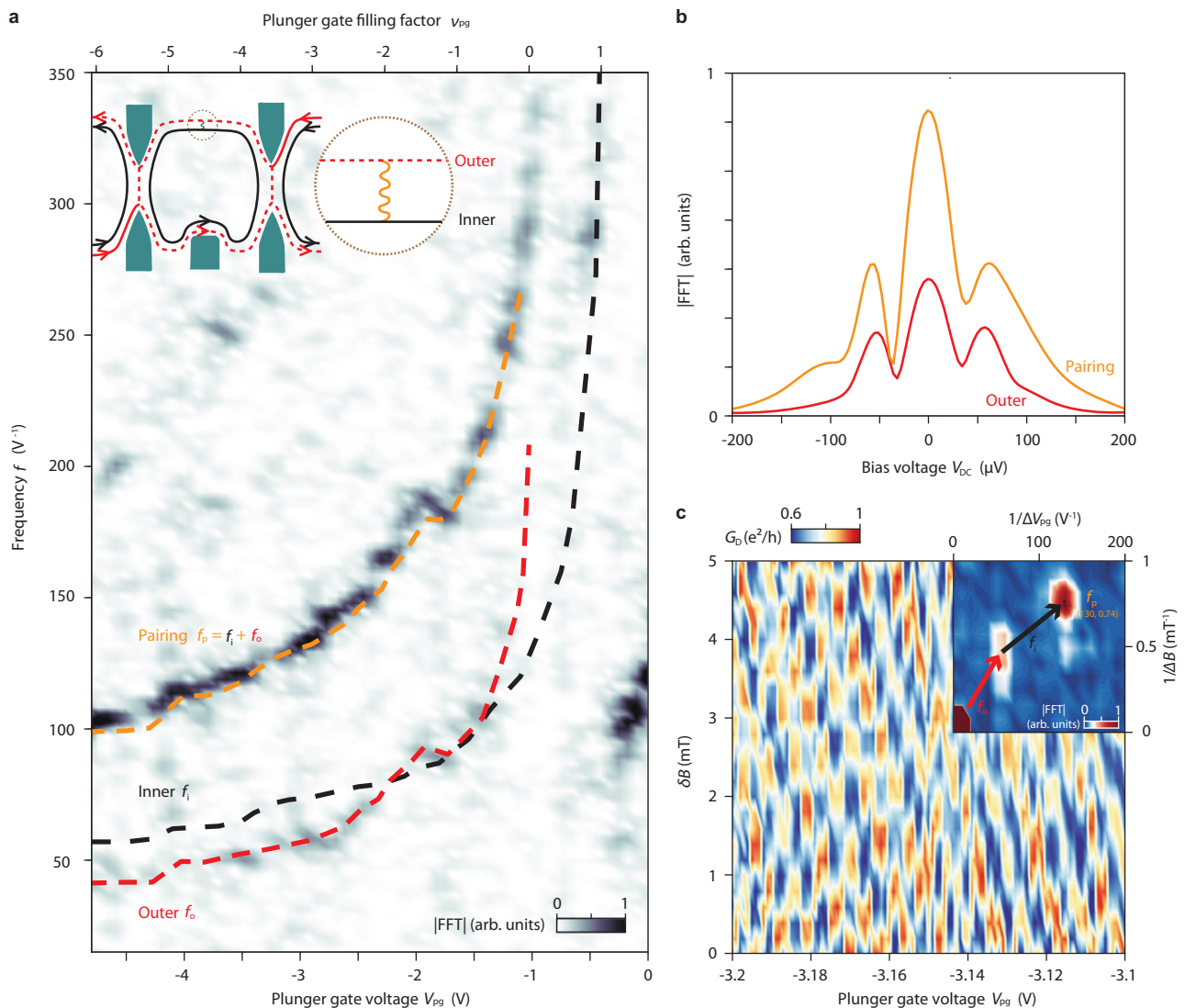


Fig. 2 | Gate-spectroscopy of outer edge channel interference. Conductance oscillations were measured by partitioning the outer edge channel with QPC transmission of $T_1 = 0.91$ and $T_2 = 0.94$ at $V_{bg} = 1.8$ V ($\nu_B = 2.26$). **a** Gate spectroscopy, FFT amplitude of the oscillation versus V_{pg} and frequency f at $V_{DC} = -55.5$ μ V. FFT is slid over the whole plunger gate voltage range with a 0.2V window. Supplementary Movie 3 shows the dependency of this gate-spectroscopy on the bias voltage. The black and red dashed lines represent the frequency dispersion of the inner f_i (determined from Fig. 1h) and outer f_o edges, respectively. The orange dashed line, calculated as the sum of f_i and f_o , coincides with the strong signal

attributed to pairing f_p . Inset schematics show the edge channel configuration, with the red dashed line indicating the partitioned outer channel and the orange wavy line representing inter-channel interaction. **b** The lobe structures of pairing (orange-colored) and the outer channel (red-colored), extracted from bias-voltage dependent gate-spectroscopy in Supplementary Movie 3. **c** The pajama map, measured at zero bias $V_{DC} = 0$ V, shows frequency beating that persists across the entire bias-voltage range (Supplementary Movie 4). Inset: 2D FFT reveals two frequencies—the outer channel f_o and pairing f_p . f_p is shown as the sum of the f_o (red arrow) and f_i (black arrow).

from the standard pattern shown in Fig. 1b. The Fourier transform reveals two contributions associated with the pairing frequency and the outer edge frequency, as shown in the inset.

Phase jumps

Taking into account these two oscillation frequencies, a simple frequency beating can describe the observed regular discontinuities. Figure 3 demonstrates how to reproduce such discontinuities in pajama maps obtained from the outer edge interference at $V_{bg} = 1.2$ V ($\nu_B = 1.7$), as illustrated in Fig. 3c.

We first simulate in Fig. 3b the oscillation of the inner channel data shown in Fig. 3a. In the data shown in Fig. 3c, a distinct negative constant phase line (see black arrows) correlates with the frequency of the bare outer channel, allowing for the extraction of its frequency, which we simulate in Fig. 3d. We then compute a signal whose frequency is the sum of the inner and outer ones in order to simulate the pairing

contribution in Fig. 3e. Adding now the pairing contribution and the outer contribution as occurring in the interferometer leads to Fig. 3f, in which a beating pattern naturally emerges and remarkably fits the data Fig. 3c.

Details regarding methods and simulations for other filling factors can be found in Supplementary Figs. 5–6. Additionally, differences in the relative weight of pairing at various bias voltages result in diverse beating patterns and apparent phase jumps²⁰, as shown in Supplementary Fig. 9j–l. This bias-dependent frequency superposition is also visualized in Supplementary Movie 4.

Similarly, the apparent complexity of the checkerboard patterns can also be fully replicated by summing those of the pairing mode and the bare outer edge, using the relative amplitude of each component extracted at zero bias. Four checkerboard patterns, shown in Supplementary Fig. 10a,c,e,g, are obtained by partitioning the outer channel at different filling factors on the $\nu_B = 2$ and $\nu_B = 3$ plateaus (e.g. pairing

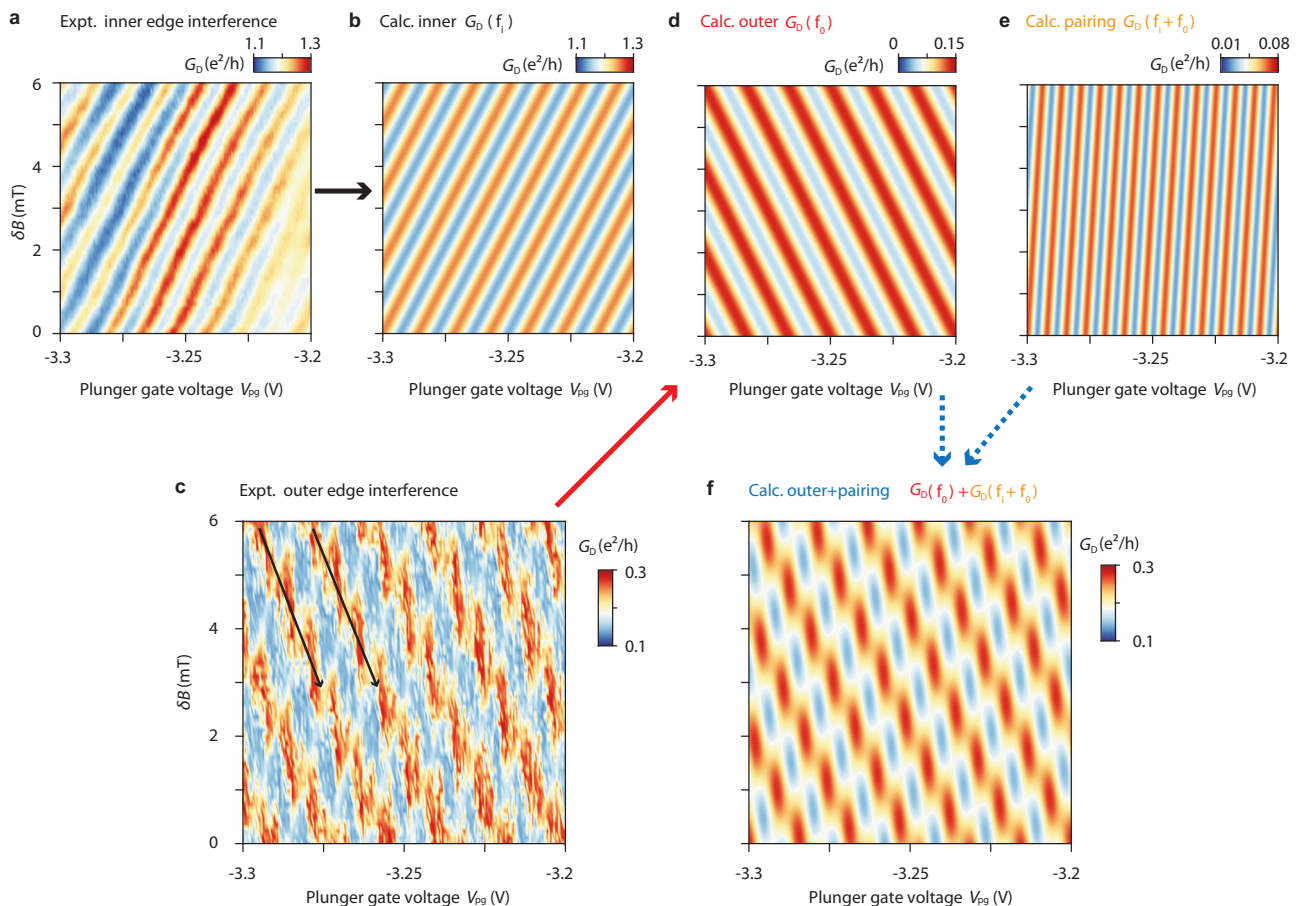


Fig. 3 | Experimental and simulated analysis of phase jumps in the pajama maps measured at $V_{bg} = 1.2$ V ($\nu_B = 1.7$). **a** The pajama map, obtained by partitioning the inner edge channel, suggests G_D oscillation with a single-frequency from the inner edge f_i . **b** Calculated pajama map with the frequency f_i derived from the panel **a**. **c** Observed pajama map when partitioning the outer edge channel, where the dominant oscillations (black arrows) provides the frequency associated with the

bare outer edge f_o . **d** Calculated pajama map using the frequency f_o . **e** The pajama map determined by pairing oscillation frequency $G_D(f_i + f_o)$. Pairing frequency is calculated by summing up f_i and f_o . **f** The diagonal conductance G_D beating in the pajama map occurs due to the simultaneous presence of two oscillations with pairing frequency $G_D(f_i + f_o)$ and outer edge frequency $G_D(f_o)$.

and tripling regime). Employing the functional form described in the Methods but considering only the first harmonic, we have successfully simulated the checkerboard patterns seen in Supplementary Fig. 10b, d, f, h, l.

Electron tripling on three coherently coupled channels

The observation of pairing naturally raises the question of whether the inclusion of an additional third channel could lead to a threefold increase in frequency, namely, electron tripling, although this has not been observed thus far in GaAs^{5,7,11,21}.

To address this question we set our QH FPI to bulk filling factor 3 and, akin to the case of pairing, we partitioned the outer channel, while having the middle and inner channels localized (Fig. 4a). Figure 4c reveals a new frequency in the plunger gate spectroscopy, highlighted with the violet dashed line, which is almost three times higher than that of the outer channel: At $V_{pg} = -3.9$ V, one finds 179 V^{-1} and 45 V^{-1} , respectively. By overlaying the spectral dispersion of the inner (black), middle (blue), and outer (red) channels, each separately identified, we can calculate the sum of the three. The violet dashed line denotes this sum and significantly aligns with the tripling frequency. As for the case of pairing, the tripling frequency therefore results from the sum of the three distinct AB phases of the three edge channels, each characterized by a different effective area.

The coherent mixing and contributions of the three channels result in a pajama pattern shown in Supplementary Movie 7 that is even

more complex than that for the pairing. Importantly, a non-negligible pairing contribution shown in the orange dashed line in Fig. 4c remains present and comes from the sum of the outer and middle channel frequencies. This suggests that pairing occurs only between the partitioned channel and the nearest neighbor channel, the middle one in this case. To ascertain this deduction, we have carried out another gate-spectroscopy in a different configuration in which we partitioned the middle channel, fully transmitted the outer channel, and localized the inner channel (see Fig. 4b). The resulting spectroscopy displayed in Fig. 4d clearly shows a pairing contribution coming from the sum of the middle and inner channels frequencies, confirming that this pairing occurs between partially transmitted and fully localized nearest neighbor channels.

Interestingly, the amplitude of the pairing peak is weaker in this configuration (also confirmed at slightly different filling factors in Supplementary Fig. 4b), while the middle and inner frequencies are visible. Here, the difference with the previous configurations at filling factor 2 is that the pairing involves channels belonging to two different Landau levels, that is, the zeroth and the first ones. Consequently, the edge channels are more spatially separated due to the large cyclotron gap compared to the case of pairing between the outer and middle edges which both belong to the zeroth Landau level. The fact that pairing intensity increases with smaller separations between channels strongly suggests that inter-channel Coulomb interactions play a crucial role in pairing and tripling.

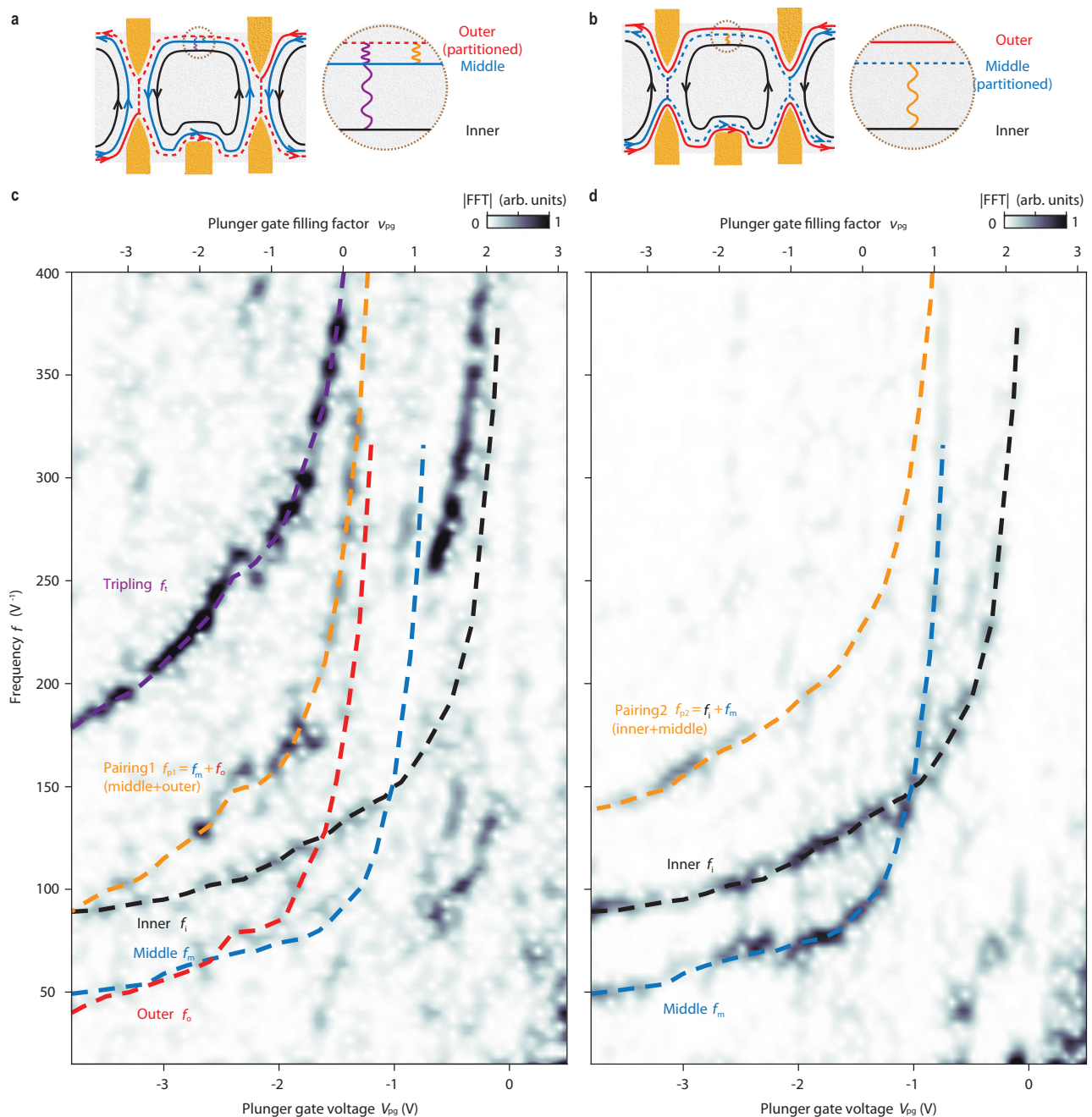


Fig. 4 | Electron tripling and pairing. **a, b** Schematic of edge channel configurations: interference with the outer channel (**a**) and the middle channel (**b**). Inner, middle, and outer edges are represented in black, blue, and red, respectively. Dashed lines denote the partitioned edges. The orange wavy line depicts the middle–outer edge interaction, and the violet wavy line illustrates the interactions among all three edges. **c** Gate spectroscopy, derived from the conductance oscillations when partitioning the outer edge channel at $V_{bg} = 2.5$ V ($v_B = 2.93$) with QPC transmission $T_1 = 0.59$ and $T_2 = 0.5$. Sliding FT was performed with a 0.45 V window. The top axis is the filling factor beneath the plunger gate. Frequencies for inner f_i , middle f_m , and outer f_o edges are marked with black, blue and red dashed lines. The orange dashed line (pairing1, f_{p1}) is the sum of f_m and f_o , and the violet dashed line (tripling, f_t) is the sum of all three channel frequencies. Data were taken

at $V_{DC} = 0$ V, with a full set of their bias voltage dependence provided in Supplementary Movie 5. Prominent signals between $1 < v_{pg} < 2$ (above 250 V^{-1}) are associated with electron tripling f_t . Weaker signals at low frequencies (-100 V^{-1}) correspond to f_o and f_{p1} . In this regime, the inner edge has been already expelled from beneath the plunger gate, while the middle and outer edges remain beneath the plunger gate and are slightly displaced from the graphene crystal edge (supplementary information section VI for details). **d**, Gate-spectroscopy obtained from outer edge channel interference, with $T_1 = 0.78$ and $T_2 = 0.81$, at $V_{DC} = -55$ μ V. The orange dashed line here (pairing2, f_{p2}) corresponds to the sum of f_m and f_i . Full bias voltage–dependent gate spectroscopy is in Supplementary Movie 6. Lobe structures for all the channels are detailed in Supplementary Fig. 3.

Real-space distance between edge channels

A key question to assess the Coulomb interaction quantitatively is the real space distance between edge channels. As in optical interferometry, our gate-spectroscopy provides a very accurate measurement of the interfering path, which can in turn lead to the edge channel–to–gate

distance $\delta(V_{pg})$ by integrating the V_{pg} -dependence of an edge channel frequency (see Methods). The integration of frequency dispersion in Fig. 2a provides the representative edge distance between two channels at $v_B = 2$, as shown in Fig. 5a. Additionally, Fig. 5b displays the distances among the three edges at $v_B = 3$. Strikingly, despite a relatively smooth

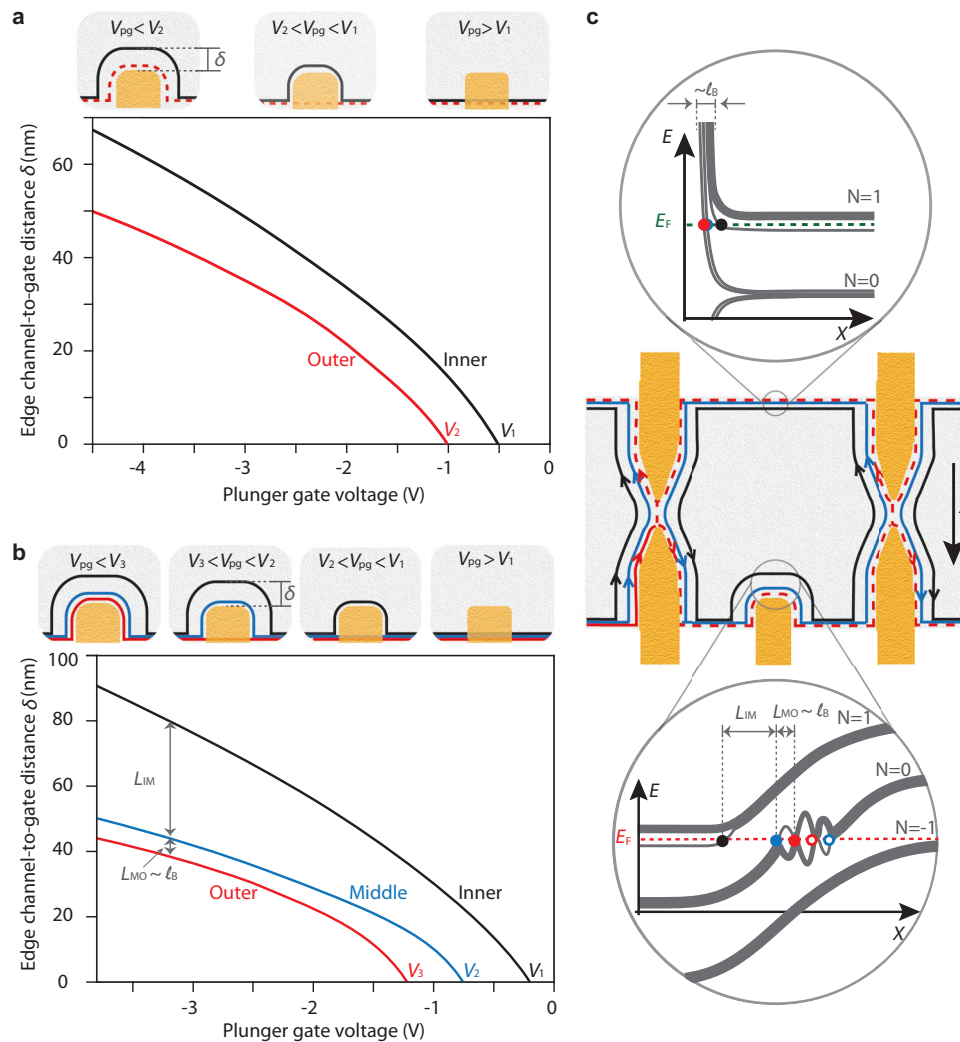


Fig. 5 | Interferometric determination of edge channel-to-plunger gate distance. **a** δ represents the distance between edge channel-to-plunger gate. Black and red lines show δ as a function of plunger gate voltage at $V_{bg} = 1.8$ V, obtained by integrating each plunger gate frequency dispersion in Fig. 2a. The top schematics illustrate edge channel configurations in three plunger gate regimes. Calculation details are in the Methods section. **b** δ for three edge channels at $V_{bg} = 2.33$ V ($\nu_B = 2.8$), derived from Fig. 4c. The distance L_{MO} between the outer and middle channels is less than a magnetic length ℓ_B , whereas the inner is at a distance $L_{IM} \sim 35$ nm from the middle due to the large cyclotron gap between the zeroth and first Landau levels. **c** The center schematic illustrates an edge configuration with a

partitioned outer edge channel (dashed red line), while the inner and middle edges are shown in the black and blue lines, respectively. The FPI is defined by gates surrounding the QPC and plunger gate (color-coded in yellow), with the crystal edge delineating the remainder. The top and bottom schematics illustrate the energy dispersion of the Landau levels along the crystal-defined and gate-defined edges, highlighting noticeable differences in edge positions. Previous studies (Refs. 18,22) have assessed the crystal edge dispersion, revealing edge channels confined to a few magnetic lengths from the crystal edge. At the pn junction, gaps of broken symmetry states open in the zeroth Landau level when the local filling factor $\nu_B(x)$ reaches every quarter filling, i.e., $\nu_B(x) = -1, 0,$ and 1 (refs. 36,37).

electrostatic potential around local top gate, the outer (red line) and middle (blue line) channels are very close, with a distance L_{MO} comparable to or even smaller than the magnetic length $\ell_B = \sqrt{\hbar/2\pi eB}$, implying strongly interacting channels. For instance, we obtain $L_{MO} = 5.6$ nm at $V_{pg} = -3$ V with a magnetic length $\ell_B = 6.7$ nm at $B = 14$ T. On the other hand, the inner channel (black line) that belongs to the first Landau level is located at $L_{IM} \sim 35$ nm (at $V_{pg} = -3$ V) away from the middle channel. This distance can be accounted for by the large cyclotron gap between the zeroth and first Landau levels of graphene. On the contrary, along the graphene crystal edges of the FPI, the QH edge channels are known to be all confined on a scale of the order of ℓ_B to the crystal edge^{18,22}. We can thus outline the spatial structure of edge channels as well as the many-body Landau level spectra at the crystal edges and the pn junctions in our FPI with the schematics in Fig. 5c. This provides novel and accurate measurements of the inter-channel distances, which are crucial for a further theoretical assessment of Coulomb interactions between the channels. It is also consistent with our

observation and interpretation of weaker pairing between the middle and inner channels at $\nu_B = 3$ discussed above.

Discussion

Inter-channel interactions typically result in fractions of the electron charge being redistributed in edge magnetoplasmons^{23–27}. For two co-propagating channels with strong mutual interactions (or with equal edge velocities), electrons decompose into fast (charged) and slow (neutral) plasmonic modes, each evolving in both channels. Their dynamics, solved through the matrix scattering approach²³ for edge magnetoplasmons, does not give rise, according to Ref. 8, to any dominant multiple electron tunneling whose contribution to dc transport vanishes at $\nu_B = 2$ and $\nu_B = 3$. A more recent theoretical work¹⁰ has taken into account charge discreteness and has considered the limit where all edges are totally pinched off at the QPCs. It has predicted that an electron entering the FPI generates neutral plasmons, so-called neutralons, which are absorbed by a second tunneling

electron; this exchange of neutralons induces a dynamical attractive interaction, thus enhancing the average Fano factor, which could potentially reach 2. In addition to the assumption of strong pinched QPCs, this enhancement requires non-universal interaction parameters, thus couldn't yet explain the robustness of pairing observed in various experimental contexts. In addition, correlated tunneling of three electrons or more is neglected as they are less probable, which seems plausible at higher filling factors as well. Note that at $\nu_B = 3$ one expects strong enough inter-edge interactions to induce two neutral modes that could enhance neutralon exchange thus pairing dynamical attraction. The present observation of tripling at $\nu_B = 3$ doesn't favor such a mechanism, and can therefore, more generally, provide a selective criterion for theoretical explanations.

A possible scenario would consist of two or three electrons entanglement mediated by inter-edge interactions. It was shown in Ref. 28 that two electrons entangled through a double dot tend to bunch in the singlet state, leading to a doubled Fano factor, but to antibunch in the triplet state. In our setup, distinguishable edge states and valley components could offer alternative degrees of freedom to the spin.

Besides, it is worth mentioning a recent report on pairwise electron tunneling into large quantum dots²⁹, reminiscent of the FPI configuration. In this context, some theoretical models predict a possible attraction-pairing-of localized electrons resulting from the minimization of the screened Coulomb interaction³⁰, and even three electrons bunching in very specific configurations³¹.

A different explanation of the frequency doubling and tripling based on charging effects^{32,33}, which has long obscured AB-dominated interferometry¹⁹, certainly deserves careful consideration. For strong capacitive coupling between the interfering edge and the bulk, designated by the Coulomb-dominated (CD) regime, and similarly to a single-electron transistor, the conductance should not depend on the magnetic field and rather oscillates with the gate voltage, which changes the occupancy of the device, leading to vertical lines in the B, V_G plane. The interfering phase varies continuously according to the relation $\theta = -2\pi\nu\phi/\phi_0$, thus is doubled or tripled at $\nu_B = 2$ or $\nu_B = 3$ respectively. In our FPI at $\nu_B = 2$, we have observed, for the inner channel, a noteworthy crossover from the CD regime to the AB regime, with an increase in the filling factor on the $h/2e^2$ quantum Hall plateau, as illustrated in Supplementary Fig. 8. Nonetheless, the pairing phenomenon gets simultaneously weaker (stronger) when the inner channel is CD (AB) (see Supplementary Fig. 8a,b,c,d). Moreover, a larger QH FPI with a size of $15 \mu\text{m}^2$ exhibits pairing exclusively at $\nu_B = 2$, without the presence of the inner or outer channel frequencies (see Supplementary Fig. 2). In that case, no signature of the CD regime is observed, most likely due to a smaller charging energy. In addition, the theoretical analysis in Ref. 32 is valid in the presence of edge reconstruction, so that highly dense localized states in compressible stripes are close enough to the edges to feel strong edge-bulk interactions. Nonetheless, we have shown the absence of edge reconstruction at the crystal edges of our devices, thus pointing towards an incompressible bulk¹⁸. Although the question remains open, these concordant observations suggest that the CD regime is not related to the pairing and tripling phenomena, in agreement with the conclusions of Ref. 5. Beyond the edge-bulk interactions, interactions between the chiral edges need to be more carefully considered and could lead us to revisit the interpretation of such a transition⁹.

A concurrent work²⁰ with a similar observation of frequency doubling proposes an explanation based on phase shifts induced by the discrete addition of charges in the inner channel strongly coupled to the outer one. The key idea is that the charge on the outer edge, which controls the FPI phase θ , is itself dependent, through inter-edge coupling, on the inner edge charge. In this model, the ground-state energy variations are expanded with respect to those of the charges on both channels. Thus, contrary to^{8,9}, the plasmonic modes are ignored; which could be justified for a short enough inner edge where

electron-hole pairs creation costs high energy. This also differs from modeling interactions by Gaussian fluctuating phase in order to fit the observed voltage dependence of the AB oscillations in Fig. 1a. In principle, one could generalize the same argument to $\nu_B = 3$. Nonetheless, we don't attribute the observed discontinuities in the pajama to phase jumps renormalized by inter-edge interactions, but rather to beating between AB oscillations of the outer channel and a pairing mode. The way these discontinuities vary with the bias voltage (see Supplementary Movie 4) would also question their emergence from a charge addition mechanism.

In addition, it is not yet established that a pure electrostatic approach could account for the electron transfer 2 by 2 observed in large quantum dots²⁹ and for shot noise measurements in interferometers based on GaAs devices^{5,7}. Indeed, for symmetric ac voltages at two QPCs, the Fano factor is given universally by the charge of the dominant tunneling process, independently on the form, strength and range of interactions, but can be increased by non-equilibrium excited states³⁴ (as in Ref. 9). The argument in Ref. 20 is also based on a well-defined charge number for the outer edge, which is questionable for almost open QPCs for which pairing has been observed as well⁷. Therefore, correlated phenomena beyond this electrostatic approximation might enter into play in this electron pairing and tripling observed in QH interferometers.

Methods

Sample fabrication

The hBN-encapsulated graphene heterostructure was assembled from exfoliated flakes using the van der Waals pick-up technique¹⁷ and deposited onto a graphite flake serving as the back-gate electrode. The substrates are highly doped Si wafers with a 285nm thick SiO₂ layer. The flake thicknesses are 27 nm for the graphite, 45.5 nm for the bottom hBN, and 27.5 nm for the top hBN. Contacts and electrostatic gates were patterned using e-beam lithography, and Cr/Au was deposited for the contacts after etching the heterostructure with a CHF₃/O₂ plasma. Pd was deposited for the electrostatic gates, preceded by a slight O₂ plasma etching to remove resist residues on hBN and ensure a homogeneous electrostatic potential beneath the gate.

Measurements

All measurements were performed in a dilution fridge with a base temperature of 0.01 K at 14 T. The measurement setup and filtering are described in Refs. 12 and 22. Systematic current-voltage characteristics were measured in a four-terminal configuration as illustrated in Fig. 1a with an acquisition card (NI-6346 from National Instruments). IV curve takes about 10 s, with oversampling enabling us to average about 1000 samples per data point. The diagonal voltage drop across the interferometer was measured with a differential FET amplifier (DLPVA-100-F-D from Femto GmbH). A homemade multichannel 20-bit digital-analog converter (DAC) was used to adjust the various gate voltages, with noise levels below $7.5 \text{ nV}/\sqrt{\text{Hz}}$, and a long time resolution of 1ppm. The DAC electronic includes an ultra-stable voltage reference LTZ1000 from Linear Technology. Differential resistance data were obtained by numerically differentiating the current-voltage characteristics.

Checkerboard pattern

In the presence of a single harmonic numbered n , the oscillation dependence with bias voltage can be described by the functional form¹²:

$$G_n^{\text{osc}} = A_n \left[\beta \cos \left(n \times \left(2\pi \frac{\phi}{\phi_0} - \frac{2L}{\hbar v} eV\beta \right) \right) + \bar{\beta} \cos \left(n \times \left(2\pi \frac{\phi}{\phi_0} + \frac{2L}{\hbar v} eV\beta \right) \right) \right] \exp \left(-\frac{(eV)^2}{\sigma_n^2} \right), \quad (1)$$

where β and $\bar{\beta}$ are asymmetry parameters describing how symmetric is the voltage drop on the two sides of the interferometer. A_n is the n th harmonic oscillation amplitude. eV is the voltage applied between the source and drain. L is the length of the interfering channel between two QPCs, v is the edge channel velocity, and φ is the AB flux picked up by the electrons. The phenomenological Gaussian energy decay describing phase fluctuations of the interfering edge channel due to Coulomb interactions or the electric noise in the non-interfering edge channels³⁵ fits best our data. The checkerboard pattern in Fig. 1e is very well reproduced by the sum of the three first harmonics $G^{\text{osc}} = \sum_n G_n^{\text{osc}}$, with $\beta = 0.4$, $\bar{\beta} = 0.6$, $A_1 = 0.25e^2/h$, $A_2 = 0.052e^2/h$, $A_3 = 0.0125e^2/h$, $\sigma_1 = 100 \mu\text{eV}$, $\sigma_2 = 80 \mu\text{eV}$, and $\sigma_3 = 65 \mu\text{eV}$, as shown in Fig. 1f. In the presence of several edge channel contributions to the oscillations, the oscillation dependence of edge channel i with bias voltage can be described by:

$$G_i^{\text{osc}} = A_i \left[\beta_i \cos \left(2\pi \frac{\varphi_i}{\phi_0} - \frac{2L}{\hbar v_i} eV \beta_i \right) + \bar{\beta}_i \cos \left(2\pi \frac{\varphi_i}{\phi_0} + \frac{2L}{\hbar v_i} eV \beta_i \right) \right] \exp \left(-\frac{(eV)^2}{\sigma_i^2} \right), \quad (2)$$

with the same notation as above. Checkerboard patterns in Supplementary Fig. 10 are very well reproduced by the sum of the outer and pairing conductance $G^{\text{osc}} = G_o^{\text{osc}} + G_p^{\text{osc}}$ without harmonics.

Gate-to-edge channel distance from gate-spectroscopy

The gate-spectroscopy is a direct measure of the capacitance coupling between the gate and the interfering edge channels¹². Assuming a distance δ between the gate and the interfering channel as drawn in the left inset in Fig. 5a, the lever arm of the gate is given by $\alpha(V_{\text{pg}}) = L_{\text{pg}} \frac{d\delta(V_{\text{pg}})}{dV_{\text{pg}}}$, where $L_{\text{pg}} = 1.5 \mu\text{m}$ is the gate edge length¹². As a result, one can compute the displacement distance δ by integrating the gate-voltage dependence of the frequency of the considered channel: $\delta(V_{\text{pg}}) = \frac{\phi_0}{BL_{\text{pg}}} \int_{V_{\text{pg}}^c}^{V_{\text{pg}}} f_{\text{pg}}(V) dV$, using $\Delta A = \phi_0/B = \alpha \Delta V_{\text{pg}} = \alpha f_{\text{pg}}$. Figure 5b displays the resulting distances for the three channels at $\nu_B = 3$ computed from Fig. 4c.

Data availability

The movies related to the transport data in this manuscript are described in the supplementary information and are available at the online Zenodo repository: <https://zenodo.org/records/10420556>.

References

- Chklovskii, D. B., Shklovskii, B. I. & Glazman, L. I. Electrostatics of edge channels. *Phys. Rev. B* **46**, 4026–4034 (1992).
- Ezawa, Z. F. & Tsitsishvili, G. Quantum Hall ferromagnets. *Rep. Prog. Phys.* **72**, 086502 (2009).
- Halperin, B. I. & Jain, J. K. *Fractional Quantum Hall Effects: New Developments* (World Scientific, 2020).
- Nayak, C., Simon, S. H., Stern, A., Freedman, M. & Sarma, S. D. Non-Abelian anyons and topological quantum computation. *Rev. Mod. Phys.* **80**, 1083 (2008).
- Choi, H. et al. Robust electron pairing in the integer quantum Hall effect regime. *Nat. Commun.* **6**, 7435 (2015).
- Van Wees, B. et al. Observation of zero-dimensional states in a one-dimensional electron interferometer. *Phys. Rev. Lett.* **62**, 2523 (1989).
- Biswas, S., Kundu, H. K., Umansky, V. & Heiblum, M. Electron pairing of interfering interface-based edge modes. *Phys. Rev. Lett.* **131**, 096302 (2023).
- Ferraro, D. & Sukhorukov, E. Interaction effects in a multi-channel Fabry-Pérot interferometer in the Aharonov-Bohm regime. *SciPost Phys.* **3**, 014 (2017).
- Frigeri, G. A., Scherer, D. D. & Rosenow, B. Sub-periods and apparent pairing in integer quantum Hall interferometers. *Europhys. Lett.* **126**, 67007 (2019).
- Frigeri, G. A. & Rosenow, B. Electron pairing in the quantum Hall regime due to neutralon exchange. *Phys. Rev. Res.* **2**, 043396 (2020).
- Sivan, I. et al. Interaction-induced interference in the integer quantum Hall effect. *Phys. Rev. B* **97**, 125405 (2018).
- Déprez, C. et al. A tunable Fabry-Pérot quantum Hall interferometer in graphene. *Nat. Nanotechnol.* **16**, 555–562 (2021).
- Ronen, Y. et al. Aharonov-Bohm effect in graphene-based Fabry-Pérot quantum Hall interferometers. *Nat. Nanotechnol.* **16**, 563–569 (2021).
- Zhao, L. et al. Graphene-based quantum Hall interferometer with self-aligned side gates. *Nano Lett.* **22**, 9645–9651 (2022).
- Fu, H., Huang, K., Watanabe, K., Taniguchi, T. & Zhu, J. Charge oscillations in bilayer graphene quantum confinement devices. *Nano Lett.* **23**, 9726–9732 (2023).
- Zimmermann, K. et al. Tunable transmission of quantum Hall edge channels with full degeneracy lifting in split-gated graphene devices. *Nat. Commun.* **8**, 14983 (2017).
- Wang, L. et al. One-dimensional electrical contact to a two-dimensional material. *Science* **342**, 614–617 (2013).
- Coissard, A. et al. Absence of edge reconstruction for quantum Hall edge channels in graphene devices. *Sci. Adv.* **9**, eadf7220 (2023).
- Zhang, Y. et al. Distinct signatures for Coulomb blockade and Aharonov-Bohm interference in electronic Fabry-Pérot interferometers. *Phys. Rev. B* **79**, 241304 (2009).
- Werkmeister, T. et al. Strongly coupled edge states in a graphene quantum Hall interferometer. *Nat. Commun.* **15**, 6533 (2024).
- Nakamura, J. et al. Aharonov-Bohm interference of fractional quantum Hall edge modes. *Nat. Phys.* **15**, 563–569 (2019).
- Vignaud, H. et al. Evidence for chiral supercurrent in quantum Hall Josephson junctions. *Nature* **624**, 545–550 (2023).
- Safi, I. A dynamic scattering approach for a gated interacting wire. *Eur. Phys. J. B* **12**, 451–455 (1999).
- Pham, K.-V., Gabay, M. & Lederer, P. Fractional excitations in the Luttinger liquid. *Phys. Rev. B* **61**, 16397–16422 (2000).
- Levkivskiy, I. P. & Sukhorukov, E. V. Dephasing in the electronic Mach-Zehnder interferometer at filling factor $\nu = 2$. *Phys. Rev. B* **78**, 045322 (2008).
- Berg, E., Oreg, Y., Kim, E.-A. & von Oppen, F. Fractional charges on an integer quantum Hall edge. *Phys. Rev. Lett.* **102**, 236402 (2009).
- Inoue, H. et al. Charge fractionalization in the integer quantum Hall effect. *Phys. Rev. Lett.* **112**, 166801 (2014).
- Burkard, G., Loss, D. & Sukhorukov, E. V. Noise of entangled electrons: Bunching and antibunching. *Phys. Rev. B* **61**, R16303–R16306 (2000).
- Demir, A. et al. Correlated double-electron additions at the edge of a two-dimensional electronic system. *Phys. Rev. Lett.* **126**, 256802 (2021).
- Raikh, M. E., Glazman, L. I. & Zhukov, L. E. Two-electron state in a disordered 2D island: Pairing caused by the Coulomb repulsion. *Phys. Rev. Lett.* **77**, 1354–1357 (1996).
- Putnam Jr, R. & Raikh, M. E. Three-electron bunches in occupation of a Coulomb cluster with $N = 5$ sites. *Phys. Rev. B* **104**, 195425 (2021).
- Halperin, B. I., Stern, A., Neder, I. & Rosenow, B. Theory of the Fabry-Pérot quantum Hall interferometer. *Phys. Rev. B* **83**, 155440 (2011).
- Sivan, I. et al. Observation of interaction-induced modulations of a quantum Hall liquid's area. *Nat. Commun.* **7**, 12184 (2016).
- Safi, I. Fluctuation-dissipation relations for strongly correlated out-of-equilibrium circuits. *Phys. Rev. B* **102**, 041113 (2020).
- Roulleau, P. et al. Finite bias visibility of the electronic Mach-Zehnder interferometer. *Phys. Rev. B* **76**, 161309 (2007).

36. Liu, X. et al. Visualizing broken symmetry and topological defects in a quantum Hall ferromagnet. *Science* **375**, 321–326 (2022).
37. Coissard, A. et al. Imaging tunable quantum Hall broken-symmetry orders in graphene. *Nature* **605**, 51–56 (2022).

Acknowledgements

We thank A. Assouline, D. Basko, P. Degiovanni, B. Douçot, M. Heiblum, B. Rosenow, K. Snizhko, and E. Sukhorukov for valuable discussions. We thank F. Blondelle for technical support on the experimental apparatus. Samples were prepared at the Nanofab facility of the Néel Institute. This work has received funding from the European Union's Horizon 2020 research and innovation program under the ERC grant SUPERGRAPH No. 866365. B.S., H.S., and W.Y. acknowledge support from the QuantERA II Program, which has received funding from the European Union's Horizon 2020 research and innovation program under Grant Agreement No 101017733. K.W. and T.T. acknowledge support from the JSPS KAKENHI (Grant Numbers 20H00354, 21H05233 and 23H02052) and World Premier International Research Center Initiative (WPI), MEXT, Japan.

Author contributions

W.Y. fabricated the sample. W.Y. and D.P. performed the measurements. W.Y. and D.P. analyzed the data with the inputs of H.S., I.S., C.D., and B.S.; I.S. provided theoretical support. K.W. and T.T. supplied the hBN crystals. S.D., E.W., and F.G. provided technical support for the experiment. B.S. supervised the project. B.S., W.Y., D.P., and I.S. wrote the paper with inputs from all the authors.

Competing interests

The authors declare no competing interests.

Additional information

Supplementary information The online version contains supplementary material available at <https://doi.org/10.1038/s41467-024-54211-3>.

Correspondence and requests for materials should be addressed to Benjamin Sacépé.

Peer review information *Nature Communications* thanks the anonymous, reviewer(s) for their contribution to the peer review of this work. A peer review file is available.

Reprints and permissions information is available at <http://www.nature.com/reprints>

Publisher's note Springer Nature remains neutral with regard to jurisdictional claims in published maps and institutional affiliations.

Open Access This article is licensed under a Creative Commons Attribution-NonCommercial-NoDerivatives 4.0 International License, which permits any non-commercial use, sharing, distribution and reproduction in any medium or format, as long as you give appropriate credit to the original author(s) and the source, provide a link to the Creative Commons licence, and indicate if you modified the licensed material. You do not have permission under this licence to share adapted material derived from this article or parts of it. The images or other third party material in this article are included in the article's Creative Commons licence, unless indicated otherwise in a credit line to the material. If material is not included in the article's Creative Commons licence and your intended use is not permitted by statutory regulation or exceeds the permitted use, you will need to obtain permission directly from the copyright holder. To view a copy of this licence, visit <http://creativecommons.org/licenses/by-nc-nd/4.0/>.

© The Author(s) 2024